

# Multi-Energy, Fast Counting Hybrid CZT Pixel Detector with Dedicated Readout Integrated Circuit

Martin Clajus, Victoria B. Cajipe, Satoshi Hayakawa, Tümay O. Tümer, and Paul D. Willson

**Abstract**— A new mixed signal front-end readout electronics integrated circuit (IC) called HILDA (Hyperspectral Imaging with Large Detector Arrays) has been developed for two-dimensional CdZnTe (CZT) pixel detector arrays. The CZT array is directly bonded on top of the IC. The CZT array and the HILDA-IC have matching geometric pixel/channel structure and dimensions, a  $16 \times 16$  array of  $0.5 \text{ mm} \times 0.5 \text{ mm}$  pitch. They are mounted together using flip-chip bump bonding. The pixel detector and readout IC are designed for high-rate photon counting independently for each channel/pixel and multiple-energy binning up to eight energy bands. Therefore, eight images can be produced that represent identical slices in time and space but different energy bands. Several HILDA CZT pixel detector hybrids have been fabricated and tested. The CZT pixel detector, the readout IC and preliminary test results are presented in this paper. The main potential applications envisioned for this chip are industrial non-destructive inspection, security applications and CT scanners.

## I. INTRODUCTION

DIRECT-CONVERSION, position-sensitive x-ray detectors that are capable of detecting photons at high rates are needed in many important technologies such as medical and industrial imaging, nondestructive inspection (NDI) and evaluation (NDE), and security screening. Advanced x-ray imaging techniques can register both shape and spectral information by measuring the attenuation of x-rays through the imaged specimen as a function of photon energy. The density and composition data thus acquired enable improved material identification. This capability is useful for several medical, industrial and security applications. In medical imaging, for example, dual-energy mammography has been reported to lead to improved diagnostic accuracy [1], and dual-energy computed tomography (CT) has been proposed for use in bone densitometry [2] and to measure fat content in the liver. Besides material identification, energy-resolved imaging has also been proposed as a tool to reject low-energy scatter and thus improve image quality [4].

Over the past decade and a half, Cadmium Zinc Telluride (CZT) has emerged as the detector material of choice for X-ray imaging because it is mechanically robust, works at room temperature with excellent energy resolution and has a large atomic number ( $Z$ ), which is essential for high-sensitivity

detection of X-rays. CZT is now being produced commercially in large quantities for X-ray and gamma-ray detectors. The large number of contributions to this symposium that are related to CZT is evidence for the continued interest in this material. The performance of CZT pulse-counting detectors at high X-ray flux has long been a matter of concern, but recent years have seen significant advances in understanding and overcoming the underlying limitations [5]-[7].

The design of large-area radiation imaging systems with high spatial resolution requires the availability of compact detector and readout modules. A hybrid pixel detector, that is, a pixelated detector array flip-chip bonded directly on top of a readout IC, offers a solution for meeting this requirement. In this paper, we discuss the design and present performance data of a hybrid detector that consists of a 256-pixel CZT detector array fabricated by eV Products and of the HILDA (Hyperspectral Imaging with Large Detector Arrays) IC developed by NOVA R&D, Inc., for the readout of this detector array or others with identical pixel geometry.

## II. THE CZT DETECTOR ARRAYS

In producing the hybrid pixel detectors, we used  $16 \times 16$ -pixel CZT detector arrays with a pitch of  $0.5 \text{ mm}$  in either direction. These arrays, which were manufactured by eV Products, are described in more detail in a separate contribution to this conference [6]. The pixel size is  $405 \mu\text{m} \times 405 \mu\text{m}$ ; the array is surrounded by a  $0.17 \text{ mm}$  wide guard ring. The resulting overall dimensions of the CZT crystal are  $8.7 \text{ mm} \times 8.7 \text{ mm}$ ; the detector thickness is  $3 \text{ mm}$ .

To facilitate testing of the detector arrays before they are bonded to readout ICs, the CZT crystals were mounted on ceramic substrates. Filled vias connect each detector pixel pad to the corresponding input pad on the readout chip. The ceramic extends beyond the crystal by  $1.95 \text{ mm}$  on one side. This overhang allows for easier handling of the arrays; it also provides room for a pair of guard ring connection pads. Fig. 1 shows photographs of the top and bottom sides of a detector array.

The detector arrays were tested prior to delivery by eV Products at count rates up to approximately one million photons per second per pixel. Details of the test procedure and of uniformity and linearity corrections applied to the data are discussed in [6].

---

Manuscript received November 17, 2006. This work was supported by the U.S. Department of Defense under the following contracts: DAAE30-02-C-1015, DAAE30-02-C-1027, and DAAE30-03-C-1074.

M. Clajus, V. B. Cajipe, S. Hayakawa and T. O. Tümer are with NOVA R&D, Inc., Riverside, CA 92507 USA (telephone: 951-781-7332, first author e-mail: martin.clajus@novarad.com).

P. D. Willson is with the U.S. Army RDECOM-ARDEC, Picatinny Arsenal, NJ 07806 USA.

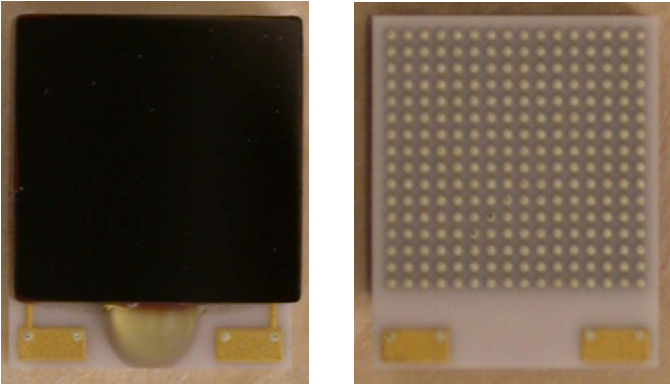


Fig. 1. Photographs of the CZT (left) and substrate sides (right) of a detector array.

### III. THE HILDA READOUT IC

The HILDA IC was developed to allow fast multi-energy readout of the detector arrays described above. Key design specifications for HILDA were previously summarized in [8]; some initial test results are presented in [9]. The chip features an array of  $16 \times 16$  readout channels with a 0.5 mm pitch, mirroring the geometry of the detector array. Each channel consists of a charge-integrating, self-resetting input amplifier, a gain amplifier, eight comparators followed by 16-bit counters, and interface circuitry for reading the counter values.

Fig. 2. shows a block diagram of a HILDA channel. The input amplifier design is optimized for a detector capacitance of 0.5 pF. The transconductance of the active feedback element ( $g_m$  in Fig. 2) is adjustable through an externally supplied bias current,  $I_{tau}$ . This allows us to continuously vary the output pulse width, measured at one tenth the peak amplitude, between approximately 100 ns and 1.3  $\mu$ s. Two signal ranges, 200 keV and 600 keV nominal, can be selected by switching the capacitors in the feedback path.

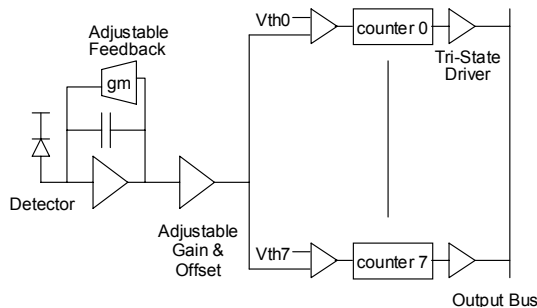


Fig. 2. Block diagram of a HILDA channel. From left to right, the diagram shows the charge-sensitive input amplifier, gain amplifier, comparators, counters and the tri-state output drivers for the counter data.

The gain stage that follows the input amplifier has adjustable offset and gain to compensate for pixel-to-pixel differences of the detector signal and leakage current and for process variations that affect the uniformity of the channel response. The offset is controlled by an eight-bit DAC with a step size that is proportional to an externally supplied reference voltage,  $V_{RI}$ ; the proportionality factor is

1.5 mV/V. The gain adjustment has six bits and a response function of the form  $gain(x) = a/(b-x)$ . The range of nominal gain values is 5.4 to 14.

The threshold voltages for the eight comparators are common to all 256 channels and are user-controlled. The threshold offsets are calibrated automatically to minimize threshold variations between the comparators. This calibration takes place whenever the counters are not enabled.

The counters record all pulses whose amplitude exceeds the corresponding comparator threshold. The counters are read out sequentially by channel, and by counter within each channel. To minimize the dead time associated with the readout in cases where fewer than eight comparator levels are needed, the reading of counters for the higher levels can be skipped. Similarly, any number of channels at the beginning or end of the sequence can be omitted from the readout. For further dead time reduction, the user can choose to disable only the counters in the channel that is being read at any given time; this comes at the expense of having each channel represent a slightly different exposure window.

The HILDA IC provides several test features. An AC-coupled test signal input can be connected to any combination of channels. The gain amplifier output from any one channel can be observed on a buffered analog monitor output. In addition, dedicated I/O pads provide buffered access to the input amplifier signals from two (fixed) channels.

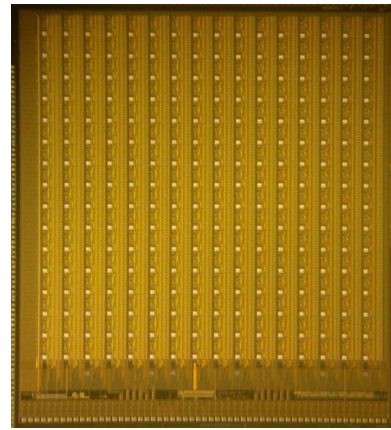


Fig. 3. Photograph of a HILDA IC.

Fig. 3 shows a photograph of a HILDA IC. The  $16 \times 16$ -array of detector input pads, each of which measures  $94 \mu\text{m} \times 94 \mu\text{m}$ , is clearly visible. The area below the channel array contains global circuits, including readout and configuration logic and bias generation for the chip's analog circuits. All I/O pads other than the detector input pads are located along the bottom edge of the die. This geometry leaves the three other sides of the chip open for tiling, with only minimal gaps as required by the detector guard rings and to accommodate mechanical tolerances. The overall chip dimensions are  $8.575 \text{ mm} \times 9.535 \text{ mm}$ .

#### IV. TEST RESULTS

The HILDA performance was characterized extensively prior to mounting any of the CZT detector arrays on top of the chips. The offset DAC response was determined by measuring the signal baseline voltage at the chip's analog monitor output as a function of DAC value. The measurement was repeated for all channels on the first two chips tested and for several randomly selected channels on subsequent chips. The response is highly linear; the  $R^2$  value is above 0.9997 for all channels. The slope of the offset curves, averaged over all channels, is  $(3.0 \pm 0.1)$  mV if VRI is set to 2 V.

To measure the combined response of the input and gain amplifiers, we connected the HILDA channels to the chip's test input and injected voltage steps of a known amplitude at a fixed rate. By varying the threshold of one of the comparators and measuring the count rate of the associated counter as a function of the threshold, we determined the amplitude at the output of the gain amplifier. Fig. 4 and Fig. 5 show typical examples of this amplitude response as a function of the gain

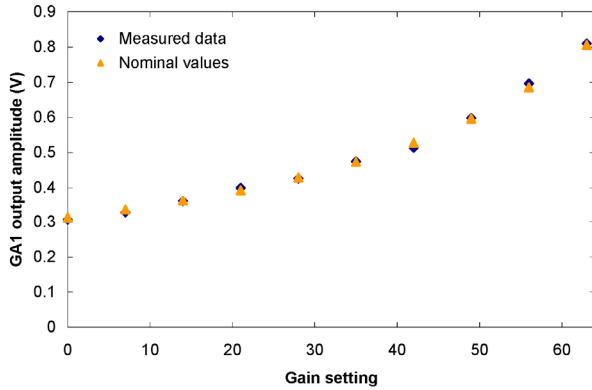


Fig. 4. Signal amplitude measured at the output of the gain amplifier (GA1), as a function of the gain setting. The input amplifier was set to the 200 keV range; the amplitude of the input signal was equivalent to a charge of 5 fC. The measured values are indicated by the blue diamonds; the yellow triangles show the nominal gain values, scaled by a common normalization factor that was determined via a least-squares fit.

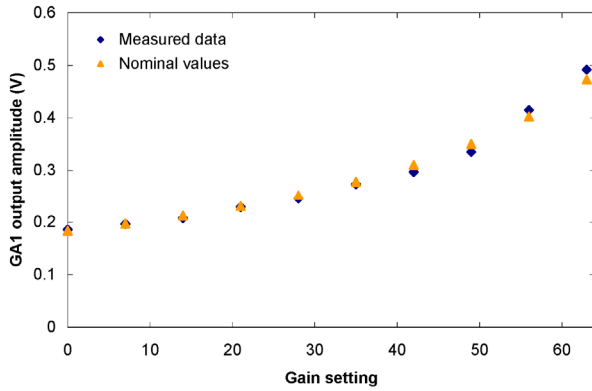


Fig. 5. Signal amplitude measured at the output of the gain amplifier (GA1), as a function of the gain setting. The input amplifier was set to the 600 keV range; the amplitude of the input signal was equivalent to a charge of 10 fC. The measured values are indicated by the blue diamonds; the yellow triangles show the nominal gain values, scaled by a common normalization factor that was determined via a least-squares fit.

setting, for the input amplifier's 200 keV and 600 keV ranges, respectively. The input amplitudes, expressed in terms of the charge on the test input coupling capacitors, were 5 fC and 10 fC, respectively. In both cases, the feedback control current  $I_{\text{tau}}$  was set to  $5 \mu\text{A}$ , which resulted in a pulse width between 300 ns and 350 ns. The measured data, indicated by the blue diamonds, agree well with the nominal gain values (yellow triangles), which were scaled by a normalization factor that is common to all data points for a given channel, input amplitude and range setting. If we ignore possible differences between the nominal and true gain of the gain amplifier, this normalization factor represents the amplitude at the output of the charge-sensitive input amplifier. For the 200 keV range, the average input amplifier gain calculated from these data is  $(10.9 \pm 0.5)$  mV/fC; the corresponding value for the 600 keV range is  $(3.5 \pm 0.2)$  mV/fC. Both values are consistent with the results of direct measurements obtained from the two channels that have input amplifier test points.

To determine the chip's noise performance, we used the same measurement procedure as we did in obtaining the gain data above, but focused our analysis on the threshold region where the counters transition from counting all pulses to not counting any. Fig. 6 shows an example of the data from this region, obtained for an input amplitude of 5 fC with the input amplifier set to the 200 keV range. The counter values obtained for different comparator thresholds are indicated by the blue diamonds; red squares denote the count differences between successive threshold steps. The count values are indicated on the left axis, the differences on the right axis. Due to noise, the transition is not abrupt but gradual, and the count differences exhibit a Gaussian distribution. The red curve shows a Gauss fit to the count differences. The width (sigma) of this fit is a measure of the channel's noise performance. Averaging again over all channels investigated, we obtain an input-referred rms noise value of  $(530 \pm 30)$  electrons.

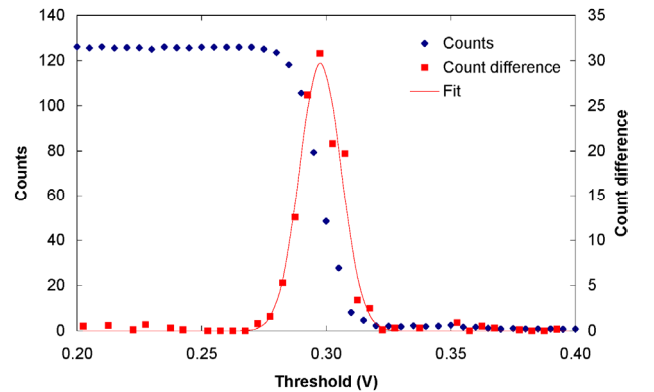


Fig. 6. Counter values (blue diamonds) as a function of threshold voltage and count differences between successive threshold steps (red squares), measured in the transition region from full counting to no counts. The red curve shows a Gauss fit to the count differences. The count values are indicated on the left axis, the differences – both data and fit – on the right axis. The threshold voltage is expressed relative to the signal baseline.

After bonding a detector array to a HILDA IC, we placed the detector hybrid in the beam of a Pantak HF-160 X-ray generator operating at 160 kVp. Two comparators and counters were used to create a window discriminator by setting their thresholds 10 mV apart and subtracting the counts obtained at the higher threshold from those for the lower threshold. Varying the thresholds of this window discriminator allowed us to measure the spectrum of the X-ray generator. Fig. 7 presents three of these spectra, measured with the same detector pixel at different amplifier gain settings as indicated in the legend. The spectrum for the lowest gain exhibits a shoulder, which we have indicated by the blue arrow. The same shoulder also shows up in the spectra from most other pixels and in those obtained at higher gain, though it is less pronounced in this case because the wider spectrum reduces the statistical accuracy of each individual bin. This consistency allows us to identify the structure as the tungsten K-edge from the X-ray tube's anode.

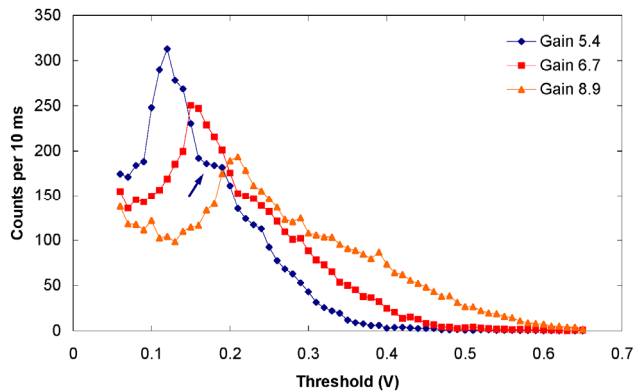


Fig. 7. Spectra of an X-ray generator operating at 160 kVp, obtained from the same detector pixel at three different amplifier gain settings. The blue arrow points to the tungsten K-edge in the spectrum recorded at the lowest gain, where this feature is clearly discernible.

We obtained these spectra for a total of seven different gain settings. We then determined the peak position in each of the seven spectra and plotted this position in Fig. 8 as a function

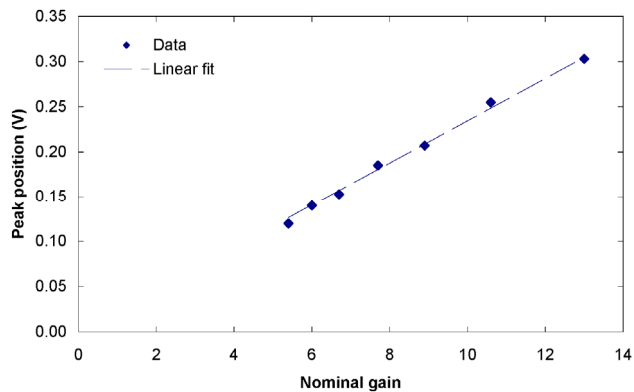


Fig. 8. Position of the peaks in the measured X-ray spectra as a function of the nominal amplifier gain. The data, indicated by the blue diamonds, are for the same pixel as the spectra in Fig. 7. The dashed line shows a linear fit to the data in which the intercept was set to zero.

of the nominal gain value. The data are fit nicely by a straight line, whose intercept is statistically consistent with zero. This result confirms the good agreement between measured and nominal gains that we already observed in the test signal data in Fig. 4 and Fig. 5.

Finally, we measured the detector response as a function of X-ray flux simultaneously for four comparator levels. The thresholds are indicated in Fig. 9 by the colored vertical lines, which are superimposed on the spectrum that matches the pixel and gain setting used in the measurement. Fig. 10 shows the flux response curves for these four threshold levels; the colors of the data symbols are the same as those of the corresponding markers in Fig. 9. The feedback control current was set to the same value, 5  $\mu$ A, that we had used in the test signal measurements. As mentioned above, this corresponds to a pulse width of 300 ns to 350 ns, so the measured maximum count rate of just under one million counts per second is pretty much in line with what should be expected for this setting.

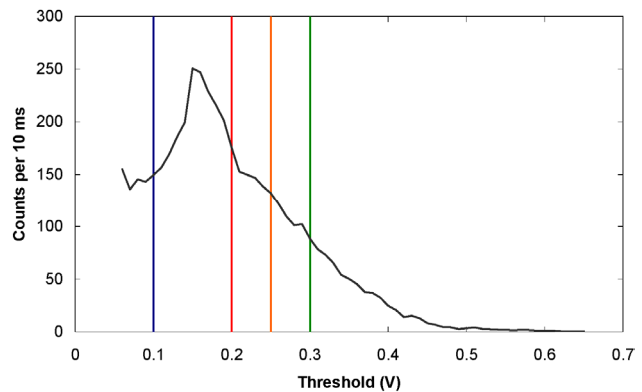


Fig. 9. The vertical lines indicate the threshold voltages for comparator levels 0 (blue), 1 (red), 2 (yellow), and 3 (green) that were used in measuring the detector response as a function of X-ray flux. The black curve represents the spectrum for the same pixel and gain setting that were used in obtaining the data in Fig. 10.

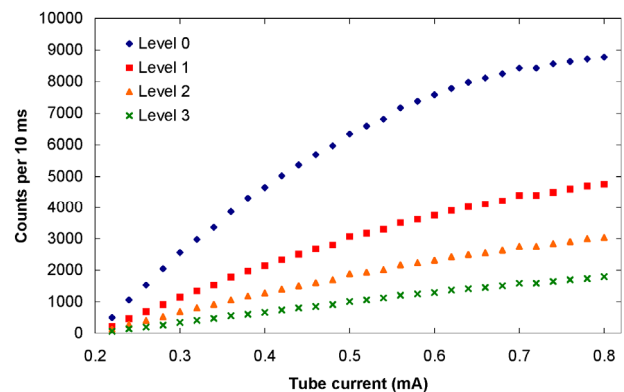


Fig. 10. Detector count rate as a function of X-ray tube current measured simultaneously for four comparator levels. The colors of the data symbols match those of the corresponding threshold markers in Fig. 9. Note that for the X-ray generator that was used in this measurement, the flux reaches zero for a current setting of approximately 0.2 mA, and the tube turns off if the setting is lower than that.

## REFERENCES

- [1] T. Asaga, C. Masuzawa, A. Yoshida, and H. Matsuura, "Dual-energy subtraction mammography," *J. Digit. Imaging*, vol. 8, pp. 70-3, February 1995.
- [2] C. E. Cann, "Quantitative CT for determination of bone mineral density: a review," *Radiology*, vol. 166, pp. 509-22, February 1988.
- [3] V. Raptopoulos et al., "Value of dual-energy CT in differentiating focal fatty infiltration of the liver from low-density masses," *Am. J. Roentgenol.*, vol. 157, pp. 721-5, October 1991.
- [4] P. Willson, M. Clajus, T. O. Tümer, G. Visser, and V. Cajipe, "Imaging Using Energy Discriminating Radiation Detector Array," *AIP Conf. Proc.*, vol. 680, p. 913, 2003.
- [5] M. Clajus et al., "CdZnTe Detectors for High-Flux X-Ray Imaging," in *Proc. 7th Int. Conf. on Appl. of Nucl. Techniques, Rethimno, Greece, July 2001*.
- [6] C. Szeles, " CdZnTe semiconductor detectors for spectroscopic X-ray imaging," *these proceedings*.
- [7] D. S. Bale and C. Szeles, "The Nature of Polarization in Wide-Bandgap Semiconductor Detectors under High-Flux Irradiation: application to CdZnTe," *these proceedings*.
- [8] T. O. Tümer et al., "New Readout Integrated Circuits for Position Sensitive Solid State Detectors," *Proc. 2004 IEEE Nucl. Science Symp., Rome, Italy, October 2004*.
- [9] T. O. Tümer, V. B. Cajipe, M. Clajus, S. Hayakawa, and A. Volkovskii, "High-resolution imaging 1D and 2D solid state detector systems," *Proc. SPIE*, vol. 6319, p. 63190P, August 2006.